The Astrophysical Journal, 988:41 (13pp), 2025 July 20 https://doi.org/10.3847/1538-4357/addfdb
© 2025. The Author(s). Published by the American Astronomical Society.
OPEN ACCESS

Bright Bursts with Submillisecond Structures of FRB 20230607A in a Highly Magnetized Environment

DeJiang Zhou[1], J. L. Han[1,2], Bing Zhang[3,4], WeiWei Zhu[1,5], Wei-yang Wang[6,7], Yuan-Pei Yang[8,9], Yuanhong Qu[3,4], Yong-Kun Zhang[1,6], Yi Yan[1,6], Wei-Cong Jing[1,6], Shuo Cao[6,10], Jintao Xie[11,12], Xuan Yang[13,14], Shiyan Tian[15], Ye Li[13], Dongzi Li[16], Jia-Rui Niu[1,6], Zi-Wei Wu[1], Qin Wu[17], Yi Feng[11,18], Fayin Wang[17,19], and Pei Wang[1]

[1] National Astronomical Observatories, Chinese Academy of Sciences, Beijing 100101, People's Republic of China; hjl@nao.cas.cn
[2] Key Laboratory of Radio Astronomy and Technology, Chinese Academy of Sciences, Beijing 100101, People's Republic of China
[3] Nevada Center for Astrophysics, University of Nevada, Las Vegas, NV 89154-4002, USA; bing.zhang@unlv.edu
[4] Department of Physics and Astronomy, University of Nevada, Las Vegas, NV 89154-4002, USA
[5] Institute for Frontiers in Astronomy and Astrophysics, Beijing Normal University, Beijing 102206, People's Republic of China
[6] School of Astronomy and Space Science, University of Chinese Academy of Sciences, Beijing 100049, People's Republic of China
[7] Department of Astronomy, School of Physics, Peking University, Beijing 100871, People's Republic of China
[8] South-Western Institute for Astronomy Research, Yunnan University, Kunming, Yunnan 650504, People's Republic of China
[9] Purple Mountain Observatory, Chinese Academy of Sciences, Nanjing 210023, People's Republic of China
[10] Yunnan Observatories, Chinese Academy of Sciences, Kunming 650216, People's Republic of China
[11] Research Center for Astronomical Computing, Zhejiang Laboratory, Hangzhou 311100, People's Republic of China
[12] School of Computer Science and Engineering, Sichuan University of Science and Engineering, Yibin 644000, People's Republic of China
[13] Purple Mountain Observatory, Chinese Academy of Sciences, Nanjing 210008, People's Republic of China
[14] School of Astronomy and Space Sciences, University of Science and Technology of China, Hefei 230026, People's Republic of China
[15] Department of Astronomy, School of Physics, Huazhong University of Science and Technology, Wuhan 430074, People's Republic of China
[16] Cahill Center for Astronomy and Astrophysics, California Institute of Technology, Pasadena, CA, USA
[17] School of Astronomy and Space Science, Nanjing University, Nanjing 210093, People's Republic of China
[18] Institute for Astronomy, School of Physics, Zhejiang University, Hangzhou 310027, People's Republic of China
[19] Key Laboratory of Modern Astronomy and Astrophysics, Nanjing University, Nanjing 210093, People's Republic of China
Received 2024 October 17; revised 2025 April 10; accepted 2025 April 11; published 2025 July 11

Abstract

We report the observations of a repeating FRB 20230607A for 15.6 hr spanning 16 months using the Five-hundred-meter Aperture Spherical Radio Telescope with the detection of 565 bursts. We present three bright bursts with detailed temporal/spectral structures. We also report that one burst carries a narrow component with a width of only 0.3 ms, which is surrounded by broader components. This suggests that repeaters can make both narrow and broad components in one burst. With the narrow spike, we precisely measure the dispersion measure of 362.85 ± 0.15 pc cm^{-3} and the Faraday rotation measures (RMs) of -12249.0 ± 1.5 rad m^{-2}. We also analyze the statistical distribution of the burst parameters, including waiting times, temporal widths, central frequencies and frequency widths, fluences and energies, all showing typical distributions of known active repeaters. In particular, most bursts show narrow spectra with $\Delta\nu/\nu_0 = 0.125 \pm 0.001$. This fact, together with the narrow 0.3 ms spike, strongly suggests a magnetospheric origin of the FRB emission. Based on a predicted correlation between RM and the luminosity of a persistent radio source (PRS) by Yang et al., we predict that the PRS should have a specific luminosity of the order of 10^{29} erg s^{-1} Hz^{-1} and encourage a search for such a PRS.

Unified Astronomy Thesaurus concepts: Radio transient sources (2008)

Materials only available in the online version of record: figure set, machine-readable table

1. Introduction

Fast radio bursts (FRBs, D. R. Lorimer et al. 2007) are coherent radio flashes with a duration of milliseconds. Their dispersion measures (DMs) exceed the maximum DM affordable by the Milky Way (D. Thornton et al. 2013). Localizations of some FRBs have firmly placed them at cosmological distances (J. P. Macquart et al. 2020). Observationally there are two apparently different types of FRBs: repeating bursts and one-off bursts (CHIME/FRB Collaboration et al. 2019). The physical origin and emission mechanism of FRBs have remained enigmatic (B. Zhang 2023).

Sensitive observations and comprehensive investigations of the details of FRB emission provide keys to understanding the nature of FRBs. For instance, polarization measurements can elucidate whether they originate from a source with a magnetosphere (R. Luo et al. 2020; J.-C. Jiang et al. 2022; H. Xu et al. 2022; J. C. Jiang et al. 2024; J. R. Niu et al. 2024). A statistical study has shown that the bursts from repeaters exhibit more complex burst morphology and larger temporal widths compared to one-off bursts, and that some bursts have very narrow spectra (Z. Pleunis et al. 2021). Some repeating bursts have very long durations with connected pulses (CHIME/FRB Collaboration et al. 2021; D. J. Zhou et al. 2022). High-time resolution observations also revealed the microstructure of some bursts, with a timescale from nanoseconds to microseconds (W. Farah et al. 2018; K. Nimmo et al. 2021, 2022; D. M. Hewitt et al. 2023; M. P. Snelders et al. 2023). These narrow spikes can help to precisely measure the DM of some FRB bursts.

Original content from this work may be used under the terms of the Creative Commons Attribution 4.0 licence. Any further distribution of this work must maintain attribution to the author(s) and the title of the work, journal citation and DOI.

When a large sample of repeated bursts is detected, the energy distributions of bursts can be analyzed (D. Li et al. 2021; H. Xu et al. 2022; Y.-K. Zhang et al. 2022, 2023). Statistics of the FRB energy distribution may be related to source energy release processes. For example, based on the observational data of FRB 20121102A from the Arecibo telescope, a high-energy tail was identified beside the main peak in the energy distribution (J. N. Jahns et al. 2023). Such high-energy bursts have been also detected for FRB 20201124A (F. Kirsten et al. 2024), FRB 20220912A (D. C. Konijn et al. 2024), and FRB 20200120E (S. B. Zhang et al. 2024).

Polarization measurements of FRBs provide special constraints of the FRB sources and environments. The extremely large Faraday rotation measures (RMs) of the two well-known repeating FRBs, FRB 20121102A (S. Chatterjee et al. 2017; D. Michilli et al. 2018) and FRB 20190520B (C. H. Niu et al. 2022; R. Anna-Thomas et al. 2023), have been detected. Incidentally, these two sources are also each associated with a persistent radio source (PRS; S. Chatterjee et al. 2017; B. Marcote et al. 2017; D. Michilli et al. 2018; C. H. Niu et al. 2022; R. Anna-Thomas et al. 2023), implying a strong synchrotron nebula in the vicinity of the FRB sources. Y.-P. Yang et al. (2020, 2022) suggested that the luminosity of the PRS should be related to the RM if the PRS is located around the FRB emission region and produces the high RM. Such a predicted correlation has been confirmed by the new observation results of FRB 20201124A, FRB 20181030A, FRB 20190407A, and FRB 202401124A (Y. Bhusare et al. 2024; G. Bruni et al. 2024a, 2024b; A. L. Ibik et al. 2024; X. Zhang & W. Yu 2024; X. Zhang et al. 2025).[20] In addition, significant variation of RM has been discussed in many repeaters, including FRB 20201124A (H. Xu et al. 2022; V. Ravi et al. 2022), FRB 20190520B (R. Anna-Thomas et al. 2023), FRB 20180916B (R. Mckinven et al. 2023a), and a few others, suggesting a dynamically evolving magnetized environment around these sources.

Recently, a new repeating FRB, FRB 20230607A, was discovered by CHIME and reported by the CHIME/FRB Virtual Observatory Event (VOEvent) Service.[21] Sensitive observations can reveal the properties of FRBs. The Five-hundred-meter Aperture Spherical radio Telescope (FAST, R. Nan 2006), with the *L*-band 19-beam receiver, possesses an exceptionally high sensitivity, making it an ideal instrument for detection of numerous bursts from several FRBs (D. Li et al. 2021; J.-C. Jiang et al. 2022; C. H. Niu et al. 2022; J.-R. Niu et al. 2022; H. Xu et al. 2022; Y.-K. Zhang et al. 2022, 2023; D. J. Zhou et al. 2022; Z. Wu et al. 2024; Z.-W. Wu et al. 2024). Following the report by the CHIME/VOEvent service on 2023 October 1, we scheduled the FAST to observe and monitor it for a few months. The observation details are shown in Table 1. In total, we observed the source for 15.6 hr and detected 565 bursts, including three bright ones. In this paper, we present the observational results of FRB 20230607A and reveal its properties. A concise overview of the observations is given in Section 2, and the results and discussions are presented in Section 3. The conclusions are given in Section 4.

[20] Note that in the case of FRB 202401124A, a flaring radio source was discovered (X. Zhang & W. Yu 2024; X. Zhang et al. 2025). Long-term monitoring of the source is needed to confirm whether the source will settle down as a PRS.

[21] https://www.chime-frb.ca/voevents

2. FAST Observations and Burst Detection

FAST has an *L*-band 19-beam receiver, working in the frequency range from 1.0 GHz to 1.5 GHz (P. Jiang et al. 2020). The system temperature at this band is about 22 K. In general, the observation band of 500 MHz is channelized to 4096 frequency channels. Due to the low gain at two sides of the band, only data for an effective bandwidth of 437.5 MHz are analyzed after removing 31.25 MHz both at the high and low band edge frequencies.

2.1. FAST Observations

After receiving the low-latency alerts of two repetitive bursts from FRB 20230607A from the CHIME/FRB VOEvent Service (CHIME/FRB Collaboration et al. 2018) on 2023 October 1, we promptly proposed and then scheduled a two-hour monitor observation session on 2023 October 16 by FAST. Because of the large uncertainty of the source's position, we used the `snapshot mode` (J. L. Han et al. 2021) for observations, which covered a sky area of 0.157 square-degree around the suggested position by using four adjacent pointings of the 19 beams, 30 minutes each. In each pointing, all 19 beams track at given coordinates. Data of all $4 \times 19 = 76$ beams are recorded and then searched for single pulses in a DM range of 3–1000 pc cm^{-3} with a step of 1.0 pc cm^{-3} by using artificial intelligence techniques to identify burst signatures on DM-Time images (D. J. Zhou et al. 2023).

From the first observation session, 21 bursts were detected, including one particularly bright burst visible in several beams and even saturated in the FAST snapshot beam M07-P4. The coordinates of the burst source are then determined by using the signal-to-noise ratios (S/Ns) and the beam center positions assuming they all have the ideal responses as done in J. L. Han et al. (2021) for bright pulsars. The new coordinates of FRB 20230607A are set to be R.A. $= 21^{\rm h}53^{\rm m}35\overset{\rm s}{.}9$, decl. $= +11^\circ17'04\overset{''}{.}2$ with uncertainties of $\sigma_{\rm RA} = 3\overset{\rm s}{.}0$ and $\sigma_{\rm Dec} = 1'06\overset{''}{.}8$ (68% confidence level).

The subsequent FAST monitoring observations (see Table 1 and the timeline of Figure 1), lasted almost for one year, targeting the new coordinate by using the central beam of the FAST *L*-band 19-beam receiver in the `tracking` or `swiftcalibration` mode.

The polarization data (*XX*, X^*Y, XY^*, and *YY*) are recorded for each frequency channel in all sessions except the first snapshot observations. The periodical calibration signals with a noise-diode-signal of 1 K in amplitude and a period of 0.2 s are injected into the feed during the first minute of each observation session. Based on these calibration signals, one can derive the polarization profiles of detected bursts (P. F. Wang et al. 2023), see details below.

2.2. Burst Detection and Parameter Estimation

From the recorded data with a sample time of generally 49.152 μs FRB 20230607A, we employ the structure maximizing method (J. W. T. Hessels et al. 2019) to find the best DM based on the average profile of the bright multicomponent bursts, that is 362.85 ± 0.15 pc cm^{-3} from a narrow-component burst on 2023 November 12, which has the smallest uncertainty (see Figure 2). We then take this DM to detect other bursts. The burst profile is obtained after the data are dedispersed with this DM.

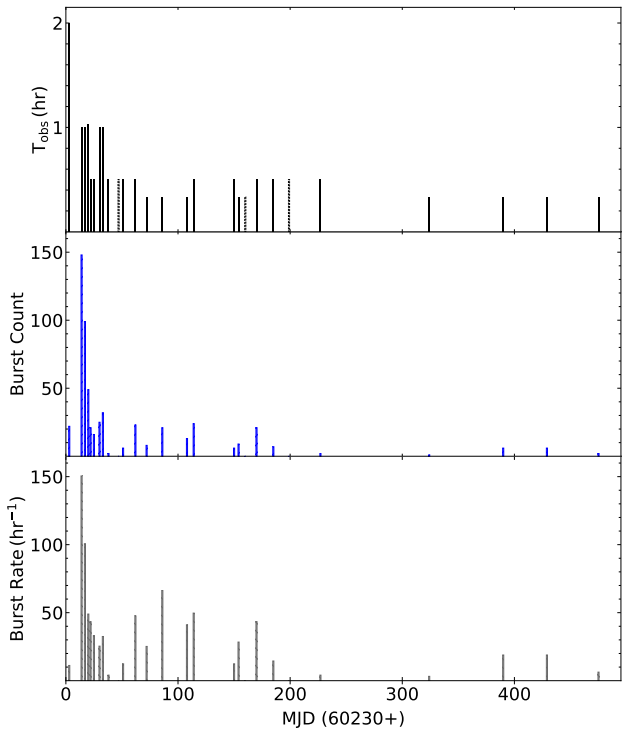


Figure 1. The observation duration of the Five-hundred-meter Aperture Spherical radio Telescope, detected burst number, and burst rate of each observation session for FRB 20230607A. The relevant parameters are listed in Table 1.

For bursts with $S/N > 7.0$, we adopt the iterative fitting methodology of D. J. Zhou et al. (2022) for the burst morphology: (1) manually set the frequency window of FAST observations; (2) perform a multi-Gaussian function fitting on the dedispersed burst profile to extract the burst components; (3) for each burst component, fit the energy distribution along the frequency channels with a Gaussian function, to get the emission frequency peak (ν_0) and the observed emission bandwidth BW_e defined by the full width at tenth-maximum (FWTM); (4) construct the refined profiles using the energy from extracted frequency channels, and (5) execute a final multi-Gaussian decomposition to establish the time-of-arrivals (TOAs), the burst temporal width (W_{sb}), and specific fluence (F_ν) for both the whole burst and the components (or say sub-bursts). Here, we take the system parameters of FAST provided by P. Jiang et al. (2020) to estimate the calibrated peak flux density (S_{peak}) and burst fluence, converting data from each bin to mJy units, with an uncertainty of approximately 20% due to system fluctuations and measurement errors.

The waiting time distribution of sub-bursts from FRB 20230607A is then obtained and shown in Figure 3, which shows two peaks. The first peak typically corresponds to intervals between different components of a burst, while the second peak represents intervals between distinct bursts. There is a valley between the two peaks at 0.5 s, separating different bursts. Such a distribution is very similar to what we have detected for other repeating FRBs by FAST (D. Li et al. 2021; H. Xu et al. 2022; Y.-K. Zhang et al. 2023). This leads us to define a burst with these emission substructures within a time-window of 0.5 s, and sub-bursts are these fine components.

3. Results and Discussions

We observed FRB 20230607A for 15.6 hr, and detected 565 bursts. The observational parameters and the number of detected bursts as well as the burst rates are listed in Table 1 and plotted in Figure 1. Most bursts are faint but three of them are very bright.

3.1. Bright Bursts

Three bright bursts were detected from FRB 20230607A on 20231016, 20231102, and 120231112, all exhibiting multi-component structures (see Figure 2). The key parameters of FRB 20230607A can be easily derived from these bright bursts, as listed in Table 2.

First is the accurate DM, which is the integration of electrons from the source to us along the path, $\mathrm{DM} = \int_0^d n_e dl$, where the n_e is the electron density, l is the unit length, and d is the distance to the source. We employed the frequency-averaged profile structure maximization method (J. W. T. Hessels et al. 2019) to get the DM values from the three bursts. Despite different complex temporal-spectrum structures, DM values from these three bright bursts from three days spanning over more than one month are consistent with each other, suggesting that the DM of this FRB does not vary significantly. From the narrowest burst detected on 2023 November 12, we get a DM with the highest precision, with $\mathrm{DM} = 362.85 \pm 0.15\ \mathrm{pc\ cm^{-3}}$.

We calibrate the polarization data of the two bright bursts detected in the tracking observations on 20231102 and 20231112. The polarization angle is computed using the formula of $\psi = 1/2\sqrt{U_i/Q_i}$. The linear polarization L_i for each data point is computed as $L_i = \sqrt{Q_i^2 + U_i^2}$. To estimate the baseline bias L_i, $|V_i|$, and the errors associated with these polarization parameters, we adopt the method described by P. F. Wang et al. (2023), and take $L_i = \sqrt{|L_i^2 - (\sigma_Q^2 + \sigma_U^2)|}$ if $L_i^2 \geqslant (\sigma_Q^2 + \sigma_U^2)$ or $L_i = -\sqrt{|L_i^2 - (\sigma_Q^2 + \sigma_U^2)|}$ for otherwise, and $|V_i| = \sqrt{|V_i^2 - \sigma_V^2|}$ if $V_i^2 \geqslant \sigma_V^2$ or $|V_i| = -\sqrt{|V_i^2 - \sigma_V^2|}$ for otherwise. We then search Faraday RMs by using the `RMSYNTH1D` and `RMCLEAN1D` of `RM-Tools` package (C. R. Purcell et al. 2020) in the range from $-20{,}000$ to $20{,}000\ \mathrm{rad\ m^{-2}}$ with a step of $1.0\ \mathrm{rad\ m^{-2}}$. We measured $\mathrm{RM_{obs}} = -12300.1 \pm 2.9\ \mathrm{rad\ m^{-2}}$ and $-12249.0 \pm 1.5\ \mathrm{rad\ m^{-2}}$ from the two bursts, as shown in Figure 4. The Faraday RM is $\mathrm{RM_{obs}} = 0.81 \int_d^0 B_{\|}(l) n_e(l) dl$, where $B_{\|}(l)$ represents the average line-of-sight magnetic field strength, measured in μG. Combining the DM and RM values, the intervening medium has magnetic fields with an average field strength of $B_{\|} = 1.232\ \mathrm{RM/DM} \simeq 42\ \mu\mathrm{G}$, with an average direction going away from us. This FRB source is located at a high Galactic latitude (GL$= 68.^\circ62$, GB$= -32.^\circ26$), and there is no such foreground Galactic cloud or intergalactic cloud of ionized gas to contribute such a DM and RM. Such a dense cloud is likely located in the host galaxy in the immediate front of the FRB source. The local magnetic field should be much stronger than 42 μG we estimated because the local DM is much smaller than the total DM we measured.

After de-Faraday rotation, we get the linear polarization of the two bursts, which has the degree of approximately $\Pi_L = L/I = \sum L_i / \sum I_i = (2.72 \pm 0.20)\%$ and $(13.81 \pm 0.24)\%$, respectively. We also measure the circular polarization degree as $\Pi_V = V/I = \sum V_i / \sum I_i = (-5.12 \pm 0.17)\%$ and

Table 1
FAST Observations of FRB 20230607A

Obs.Date/MJD	Obs.Mode	T_{obs} (min)	t_{samp} (μs)	No. of Bursts	Burst Rate (hr^{-1})	No. of Sub-bursts
(1)	(2)	(3)	(4)	(5)	(6)	(7)
20231016/60233	snapshot	118	196.608	21 (M07)	10.7	26
20231027/60244	tracking	59	98.304	147 (M05)	149.5	193
20231030/60247	tracking	59	49.152	99	100.7	138
20231102/60250	tracking	61	49.152	47	46.2	56
20231104/60252	tracking	29	196.608	21	43.4	25
20231107/60255	tracking	29	49.152	16	33.1	19
20211112/60260	tracking	59	49.152	25	25.4	41
20211115/60263	tracking	59	49.152	32	32.5	32
20231120/60268	tracking	29	49.152	2	4.1	2
20231129/60277	tracking	29	49.152	0	0.0	0
20231203/60281	tracking	29	49.152	6	12.4	7
20231214/60292	tracking	29	49.152	23	47.6	31
20231224/60302	tracking	19	49.152	8	25.2	10
20240107/60316	tracking	19	49.152	21	66.3	26
20240129/60338	tracking	19	49.152	13	41.1	14
20240204/60344	tracking	29	49.152	24	49.7	27
20240311/60380	tracking	29	196.608	6	12.4	6
20240315/60384	tracking	19	49.152	9	28.4	11
20240321/60390	tracking	19	98.304	0	0.0	0
20240331/60400	tracking	29	49.152	21	43.4	26
20240415/60415	tracking	29	49.152	7	14.5	8
20240429/60429	tracking	29	49.152	0	0.0	0
20240527/60457	tracking	29	49.152	2	4.1	2
20240901/60554	swiftcalibration	19	49.152	1	3.2	1
20241106/60620	swiftcalibration	19	49.152	6	18.9	10
20241215/60659	swiftcalibration	19	49.152	6	18.9	7
20250130/60705	swiftcalibration	19	49.152	2	6.3	2
Total	⋯	934		565	⋯	720

Note. The columns are observation date with MJD, observation mode, effective observation time in minutes, sampling time, number of bursts detected, burst rate in number per hour, and sub-burst number.

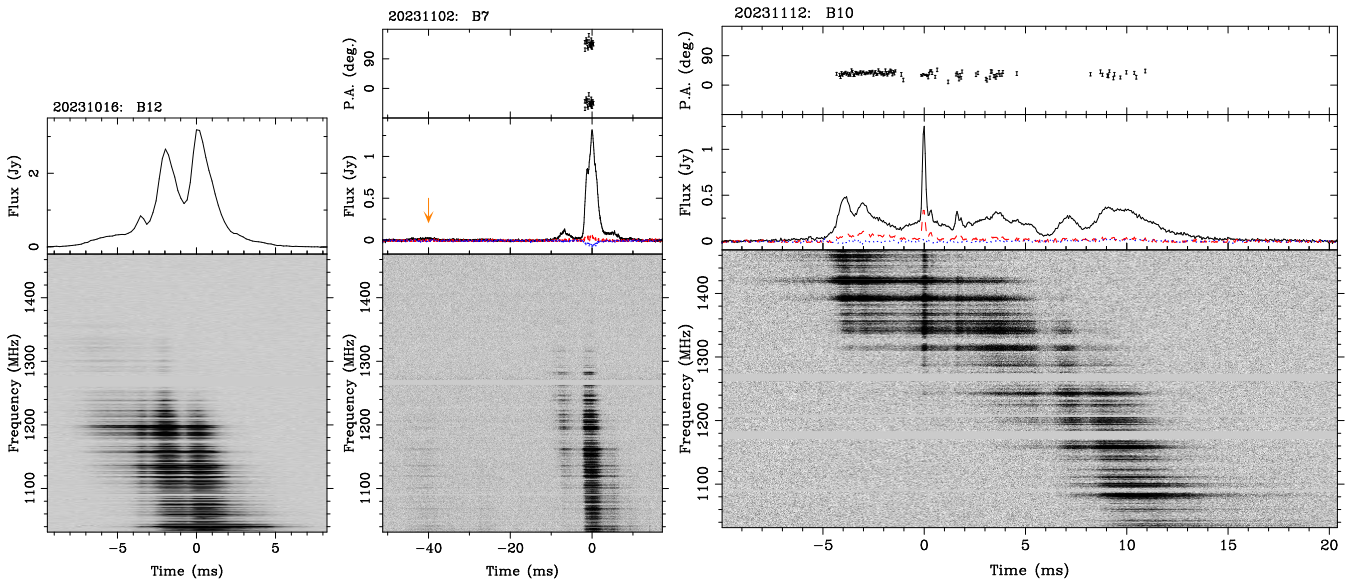


Figure 2. Three brightest bursts of FRB 20230607A. The bottom subpanels show the two-dimensional dynamic spectrum over frequency and time. The middle subpanels show the polarization profiles, solid line for total intensity I, dashed line for linear polarization L, and dotted line for circular polarization V, and the top subpanels show the polarized position angles. The observation date and burst number are marked on the top of the panels. The arrow at around −40 ms of the burst B7 on 20231102 indicates a weak emission component.

Table 2
Properties of Three Bright Bursts of FRB 20230607A

Date	20231016	20231102	20231112
Burst NO.	B12	B7	B10
TOA[a] (MJD)	60233.6029055482	60250.5562919966	60260.5286762679
DM[b] (pc cm^{-3})	363.16 ± 0.21	363.16 ± 0.28	362.85 ± 0.15
Width (ms)	12.5	36.7	36.0
Peak flux density $S_{\rm peak}$ (Jy)	$>3280.5 \pm 3.9$	1315.4 ± 7.7	1312.3 ± 7.8
Specific fluence F_ν (mJy ms)	$>34851 \pm 17$	16076 ± 30	11123 ± 64
Energy $\sum E_\nu$ ($\times 10^{39}$erg)	$>8.028 \pm 0.004$	4.129 ± 0.008	4.223 ± 0.002
$\rm RM_{obs}$ (rad m^{-2})	...	-12300.1 ± 2.9	-12249.0 ± 1.5
$\langle B_\parallel \rangle$ (μG)	...	-41.73 ± 0.04	-41.59 ± 0.02
L/I (%)	...	2.72 ± 0.20	13.81 ± 0.24
$L_{\rm peak}/I_{\rm peak}$ (%)	...	4.52 ± 0.64	26.81 ± 0.79
V/I (%)	...	-5.12 ± 0.17	1.76 ± 0.18
$\lvert V\rvert$/I (%)	...	4.45 ± 0.17	2.52 ± 0.18
$f_{\rm depol}$	...	3.18×10^{-3}	3.15×10^{-3}

Notes.
[a] TOA of each burst is referenced to the infinite frequency at the solar system barycentre by the ephemeris DE440.
[b] The DM derived from each burst.

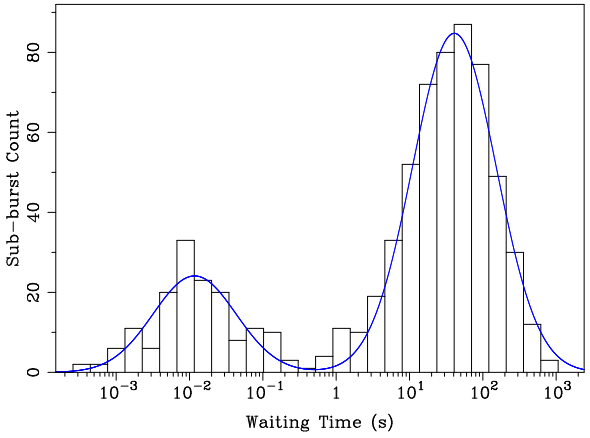


Figure 3. The distribution of waiting time of FAST detected sub-bursts from FRB 20230607A. The blue solid line represents the best-fit model with two log-normal functions with fitted peaks at 11.7 ms and 40.9 s. The minimum of the bridge is 507.6 ms.

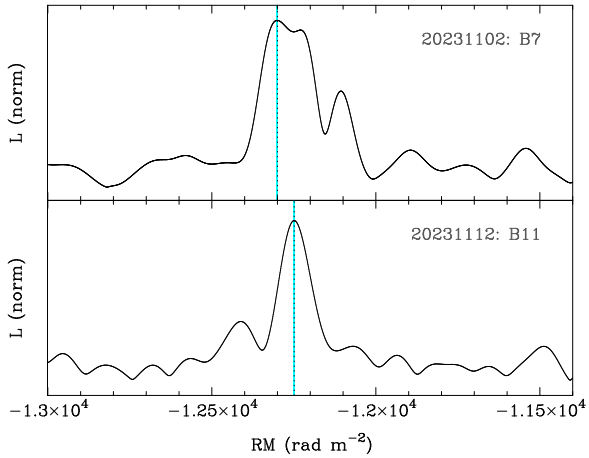


Figure 4. The RMCLEAN results of the two bursts for the RM determinations. The vertical dotted lines indicated RM values at -12300.1 rad m^2 (up) and -12249.0 rad m^2 (bottom), respectively.

$(1.76 \pm 0.18)\%$, respectively. Considering the negligible depolarization of only 0.32% caused by the RM inside the frequency channels, such low polarization degrees in the frequency range of 1.0–1.5 GHz need to be attributed to other effects. Intrinsic FRB emission mechanisms typically produce higher polarization degrees than these observations (Y. Qu & B. Zhang 2023), which are consistent with the polarization observations of other active repeaters (e.g., J.-C. Jiang et al. 2022). Even though it is not impossible that the intrinsic radiation mechanism of this source might produce lower polarization degrees, some external mechanisms, such as depolarization effect due to multipath RM variations, might be at play (P. Beniamini et al. 2022). The effect is more significant for larger RM FRBs (Y. Feng et al. 2022). FRB 20230607A has the third highest RM known, so likely suffers from such a $\sigma_{\rm RM}$ effect.

One important feature is in the bright burst (B10) observed on 2023 November 12 (Figure 2). Among many broad pulses, there is a very narrow spike. The time delay $\Delta t_{\rm chan}$ caused by DM smearing inside a channel:

$$\Delta t_{\rm chan} = 8.3\ \mu s \cdot {\rm DM} \cdot \frac{\Delta f}{\rm MHz} \cdot \left(\frac{f}{\rm GHz}\right)^{-3}, \quad (1)$$

where the channel bandwidth for FAST observations is $\Delta f = 0.1220703125$ MHz, and the f is the central frequency of the channel. The width of this narrow spike is fitted as $W_{\rm obs} \sim 0.3$ ms (see the method in Section 2.2), after ignoring the scatter-broadening effect and correcting for the DM smearing of about $\Delta t_{\rm chan} = 188\ \mu$s at 1250 MHz with the function of $W_{\rm obs} = \sqrt{W_{\rm int}^2 + t_{\rm samp}^2 + \Delta t_{\rm chan}^2}$, where the sampling time is $t_{\rm samp} = 49.152\ \mu$s, the intrinsic FWTM of this spike is only $W_{\rm int} \sim 229\ \mu$s. This timescale corresponds to a light travel

Table 3
Burst Numbers for Different Classifications for FRB 20230607A

Drifting Mode	Component Count	Burst Emerging in the FAST *L*-band			
		Whole-band	High Part	Middle Part	Lower Part
Downward: 405	one: 343 two: 58 multiple: 15	D1-W: 60 D2-W: 19 Dm-W: 9	D1-H: 41 D2-H: 3 Dm-H: 0	D1-M: 129 D2-M: 19 Dm-M: 0	D1-L: 113 D2-L: 17 Dm-L: 6
Upward: 9	⋯	⋯	⋯	U2-M: 6	U2-L: 3
Complex: 15	⋯	C: 15			
No drifting: 18	⋯	ND: 18			
No evidence: 107	⋯	⋯	NE-H: 12	⋯	NE-L: 95

distance of ∼69 km, representing an upper limit on the spatial extent of the coherent emission region for a rotating central engine, suggesting a magnetospheric origin of the emission.

Such a curious feature sheds light into our understanding of FRB emission mechanism. First, CHIME observations have suggested that repeaters and nonrepeaters seem to have statistically different emission properties. While nonrepeaters tend to have short widths, bursts of repeaters tend to be broad and often show a frequency down drift with time (Z. Pleunis et al. 2021). The B10 burst indeed has many pulses with the frequency down drift. However, even though many bursts have broad widths, the brightest one has a very narrow spike. Our observation indicates that repeaters can make both broad and narrow pulses.

Second, the distinct width difference between the narrow spike and the surrounding broader pulses constrain the FRB emission mechanism. First, the existence of a narrow spike in long-duration burst such as B10 essentially rules out any far-away models invoking relativistic shocks and synchrotron maser because a narrow spike needs a very small clump in the upstream which gives a very low radiative efficiency, which is inconsistent with the high flux of the spike (P. Beniamin & P. Kumar 2020; W. Lu et al. 2022; B. Zhang 2023). This gives yet another strong support to the magnetospheric origin of FRBs. Within the magnetospheric models, different subpulses correspond to emitters from different bundle of magnetic field lines. The sharp spike raises a challenge to such a model. One possibility is that the sharp spike and the other broader pulses originate from different emission regions, with the sharp spike coming from lower altitudes than the broader ones. Another possibility is that the narrow spike might be amplified by the caustic effect. Detailed modeling is needed to unveil the radiation geometry of this peculiar burst.

3.2. Burst Classification

There are 720 sub-bursts in all 565 bursts detected from 20230607A. Most bursts are weak but exhibit a diverse morphology: some bursts emerge in narrow-band at some random frequencies, while some bursts show frequency drifting between or within burst components.

Following the classification scheme proposed by D. J. Zhou et al. (2022), we classify the detected bursts of FRB 20230607A based on the number of components, their occurrence frequencies, and their drift states. We use "U" and "D" to indicate upward- and downward-frequency drifting; we use numbers "1," "2," and "m" to indicate the number of burst component for one, two, or multiple components, respectively; while we use "W," "H," "M," and "L" to mark the observed burst energy detected in whole (wide) FAST *L*-band, or only in higher, middle, or lower part of the frequency band, respectively. For example, the class "D1-W" means a burst with one component only detected in the whole FAST *L*-band with a downward-drifting feature. Some bursts have a complex morphology, which we classify as "C." Some bursts are detected in the water-fall plot of the frequency-time image and the pulses do not drift, and we classify them as "ND." If the data are not good enough to judge if there is a frequency drift, we classify them as "NE" for no evidence of drifting.

We checked all detected bursts and counted the burst numbers for each category, as listed in Table 3 and detailed in the Appendix in Table 4 and Figure 10. Among these 565 bursts, the majority exhibit downward-frequency drifting, with only nine bursts showing upward-frequency drifting.

3.3. Distributions of Sub-burst Parameters

We have analyzed all the bursts of FRB 20230607A in our sample and obtained all the parameters of bursts and sub-bursts. In Figure 5, the distributions of these parameters are presented. To ensure good statistics, only those sub-bursts with an emission frequency ν_0 peaked within the FAST band of 1031.25–1468.75 MHz are considered in this subsection.

As shown in Figure 5, the number of detected sub-bursts obviously decreases with the peak emission frequency ν_0, which differs from the bimodal distribution reported for FRB 20201124A detected by FAST (D. J. Zhou et al. 2022) and FRBs observed by CHIME (A. E. Lanman et al. 2022). The number distribution can be fitted by a power-law function with an index of -4.79 ± 0.32. The number distributions of $\mathrm{BW_e}$ and W_{sb} exhibit log-normal shapes, and they can be fitted with log-normal functions, with peak values at 231^{+171}_{-99} MHz and $11.4^{+10.6}_{-5.5}$ ms, respectively. The distribution of fluence F_ν (in units of mJy ms) has one main peak and a tail component for high values. We use two log-normal functions to fit the distribution, with two peaks at $\log F_\nu = 1.97 \pm 0.40$ and $\log F_\nu = 3.34 \pm 0.21$, respectively.

For the subplot of the frequency versus emission bandwidth in Figure 5, the fitted emission bandwidth narrows toward the edges of the observing band that may arise from scintillation-induced distortions in burst morphology. While our calibration and fitting procedures are robust (see Section 2.2), scintillation

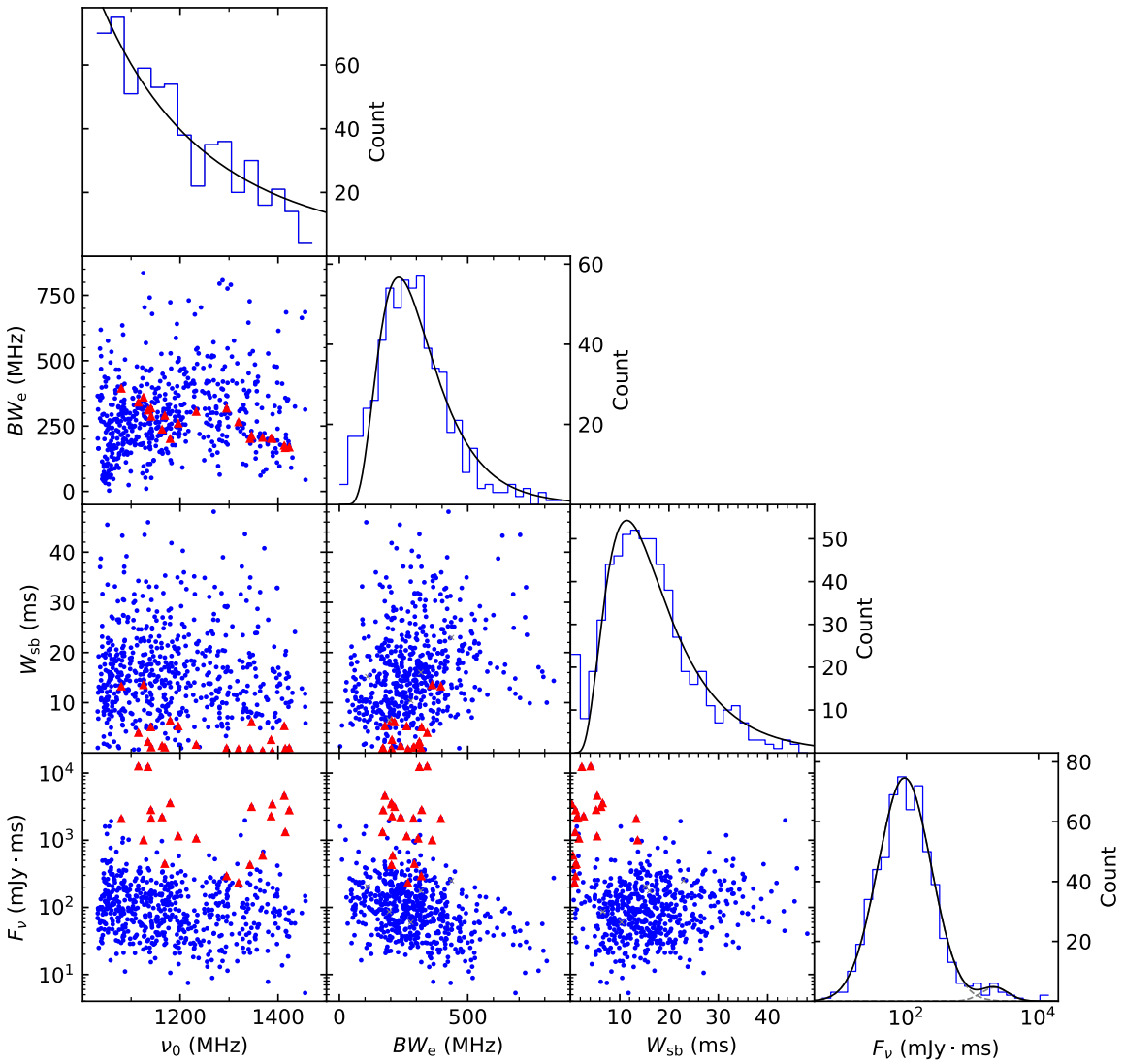


Figure 5. Parameter distribution of sub-bursts of FRB 20230607A for the emission peak frequency (ν_0 from 1031.25 MHz to 1468.75 MHz in the FAST effective observation bandwidth), derived emission bandwidth (BW_e), sub-burst temporal width (W_{sb}), and the fluence F_ν. The triangles represent the parameters from the three bright bursts, the other points correspond to those from weaker bursts. The distribution of ν_0 can be fitted with a power-law function with an index of -4.79 ± 0.32, as shown on the top subpanel. A log-normal function is used to fit the distribution of BW_e and W_{sb} which have the fitted peak of 231^{+171}_{-99} MHz and $11.4^{+10.6}_{-5.5}$ ms, respectively. Two Gaussian functions are used to fit the distribution of $\log F_\nu$ with peaks at $\log F_\nu = 1.97 \pm 0.40$ and $\log F_\nu = 3.34 \pm 0.21$.

introduces nonphysical trends in these edge regions. Its impact is confined to a small subset of bursts and does not alter our conclusions on spectral properties and burst energetics. Critically, the narrow-band bursts detected near the center of the observing band—unaffected by edge artifacts—remain statistically representative, and their inclusion ensures the validity of the overall trends.

Notice that most bursts from FRB 20230607A have the emission limited in a narrow range inside the FAST observation band, similar to other FRBs (Z. Pleunis et al. 2021; D. J. Zhou et al. 2022; Y.-K. Zhang et al. 2023). The distribution of $\Delta\nu/\nu_0$, here $\Delta\nu$ is the full width at half-maximum (FWHM, not to be confused with FWTM for the full width at tenth-maximum), is shown in Figure 6. It is almost in a Gaussian distribution with a mean of $\Delta\nu/\nu_0 = 0.125 \pm 0.001$ and a standard deviation of $\sigma = 0.060 \pm 0.001$. The narrow-band emission of FRBs, with a mean $\Delta\nu/\nu_0$ of 0.125 for FRB 20230607A, 0.13 for FRB 20220912A (Y.-K. Zhang et al. 2023), and 0.12 for FRB 20240114A (A. Kumar et al. 2024), is now a common feature of active repeating FRB sources. Even though some propagation effects such as scintillation and filamentation instability may produce narrow spectra in some bursts (P. Kumar et al. 2024), the ubiquitousness of such narrow spectra among all detected bursts suggest that they are most likely related to the intrinsic observational mechanisms. Since synchrotron maser models invoking relativistic shocks predict a minimum $\Delta\nu/\nu_0 \sim 0.58$ because of the high-latitude effect, our observations rule out these models and lend another strong support of the magnetospheric origin of FRB emission (P. Kumar et al. 2024). One attractive mechanism to produce narrow spectra in a magnetar magnetosphere invokes inverse Compton scattering of low frequency fast magnetosonic waves by relativistic particle bunches (B. Zhang 2022; Y. Qu & B. Zhang 2024). The traditional coherent curvature radiation by bunches may also achieve a narrow spectrum if the bunches are properly spaced spatially (Y.-P. Yang 2023; W.-Y. Wang et al. 2024).

Table 4
Burst and Sub-burst Parameters of FRB 20230607A

Burst No. (1)	TOA (MJD) (2)	S/N (3)	W (ms) (4)	S_{peak} (mJy) (5)	F_ν (mJy ms) (6)	ν_0 (MHz) (7)	BW_e (MHz) (8)	ν_{low} (MHz) (9)	ν_{high} (MHz) (10)	Group (11)
Date: 20231016:										
1	60233.558168477	5.0	13.0	4.3	16.0	1420.6	352.6	1244.3	1468.8	NE-H
2	60233.570489883	9.4	10.5	15.1	107.3	1046.5	97.7	1031.3	1095.3	NE-L
3	60233.571091100	7.9	11.6	5.7	24.9	1103.7	355.5	1031.3	1281.4	NE-L
4	60233.581817599	10.1	16.7	5.8	42.7	1130.3	462.9	1031.3	1361.7	D1-M
5	60233.584250617	16.6	40.8	8.2	148.1	1372.0	222.3	1260.9	1468.8	D1-H
6	60233.585737573	16.9	39.3	7.9	144.8	⋯	169.9	1031.4	1201.2	D1-L
7	60233.589840754	7.0	34.1	3.6	21.8	1130.6	277.9	1031.3	1269.6	D1-L
8	60233.593123968	21.8	47.4	17.9	360.6	⋯	95.6	1031.4	1127.0	D1-L
9	60233.597812443	6.4	16.0	4.4	25.6	1079.7	298.5	1031.3	1229.0	NE-L
10	60233.600471432	7.4	16.0	5.0	33.0	⋯	228.5	1031.4	1259.8	NE-L
11	60233.602353388	9.9	18.4	4.8	42.4	1222.9	412.5	1031.3	1429.2	D1-M
12	60233.602907196	1957.9	12.5	3710.9	14540.1	⋯	265.4	1031.4	1296.8	Dm-L
12-1	60233.602907140	368.5	6.5	519.9	3131.4	1179.6	202.7	1078.3	1280.9	⋯
12-2	60233.602907154	246.5	1.5	667.5	1929.6	1163.2	238.9	1043.8	1282.7	⋯
12-3	60233.602907173	1437.0	2.3	3021.4	10803.4	1134.5	311.6	1031.3	1290.3	⋯
12-4	60233.602907196	1246.0	2.1	2716.2	9292.0	⋯	263.2	1031.4	1294.6	⋯
12-5	60233.602907203	829.4	5.1	1158.6	6159.5	⋯	265.4	1031.4	1296.8	⋯
13	60233.605237366	10.3	25.7	16.0	206.1	1204.7	91.5	1158.9	1250.5	D1-M
14	60233.606697023	37.6	19.6	56.2	243.4	⋯	257.3	1031.4	1288.7	Dm-L
14-1	60233.606697024	26.2	2.6	55.0	204.7	1189.7	176.6	1101.3	1278.0	⋯
14-2	60233.606697052	26.3	14.5	20.0	177.0	1170.1	237.2	1051.5	1288.7	⋯
14-3	60233.606697142	28.7	5.0	65.0	338.1	1059.1	99.8	1031.3	1109.0	⋯
15	60233.607442435	7.3	18.3	4.0	25.1	1148.7	376.1	1031.3	1336.8	ND
16	60233.608604885	9.3	7.2	11.6	64.5	1393.1	194.1	1296.0	1468.8	ND

(This table is available in its entirety in machine-readable form in the online article.)

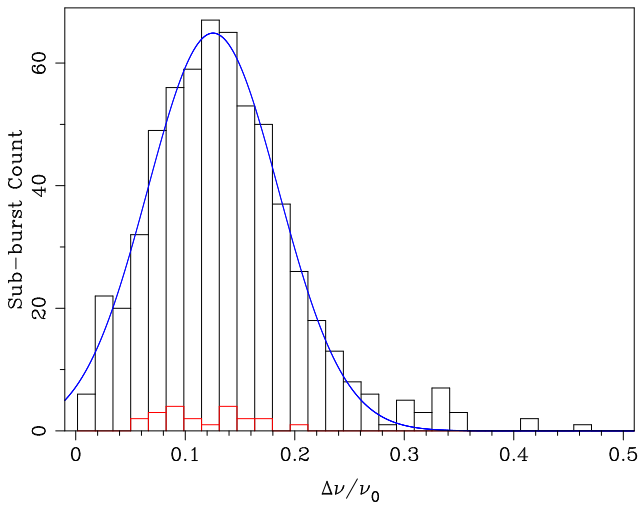


Figure 6. The fraction distribution of emission bandwidth $\Delta\nu$ of the emission frequency peak ν_0 for all the sub-bursts (black) and those in the three bright bursts (red) of FRB 20230607A. The solid line represents the best-fit model with a Gaussian function with a peak at $\Delta\nu/\nu_0 = 0.125 \pm 0.001$ and a fitted width of $\sigma = 0.060 \pm 0.001$.

3.4. The Energy Distribution

Except for the bursts detected on the first day with the snapshot mode, when the source was offset from the beam center and the scintillation effect complicated the flux analysis, the flux density of other bursts/sub-bursts can be reliably estimated from data through comparing with the system noise temperature. The fluence distribution for sub-bursts of FRB 20230607A has a prominent low-energy peak and a less conspicuous high-fluence tail (see Figure 5).

Because the host galaxy of FRB 20230607A is not known yet, before analyzing the energy of FRB events, we have to estimate the source distance from the intergalactic DM contribution. The DM contribution from the Milky Way can be estimated by using the YMW16 model (J. M. Yao et al. 2017) with $DM_{MW} = 37.8\,pc\,cm^{-3}$. The excessive DM of $DM_{extra} = 275.05\,pc\,cm^{-3}$ is attributed to contributions from the local medium and the intergalactic medium. The DM contribution from the host is unknown. Following a generic statistical constraint by Z. Li et al. (2020), the DM contribution from the host in the local galaxy frame is approximated as $DM_{host,LG} = 107^{+24}_{-45}\,pc\,cm^{-3}$. By deducting DM_{MW}, we derive the extragalactic $DM_{extra} = DM_{IGM} + DM_{host,LG}/(1+z)$ and use it to estimate the redshift z, where the DM contributed by the IGM is (W. Deng & B. Zhang 2014):

$$DM_{IGM} = \frac{3cH_0\Omega_b f_{IGM}}{8\pi G m_p}\int_0^z \frac{\chi(z)(1+z)dz}{[\Omega_m(1+z)^3+\Omega_\Lambda]^{\frac{1}{2}}}, \quad (2)$$

where $\chi(z) = 7/8$ is the free electron number per baryon in the universe and $f_{IGM} \sim 0.83$ is the fraction of baryons in the intergalactic medium, where the ΛCDM cosmological parameters are taken as $\Omega_m = 0.315 \pm 0.007$, $\Omega_b = 0.02237 \pm 0.00015$, and $H_0 = 67.36 \pm 0.54\,km\,s^{-1}\,Mpc^{-1}$ (Planck Collaboration et al. 2020). We estimate $z \sim 0.22$, which gives a luminosity distance of $D_L \sim 0.98\,Gpc$. This distance is

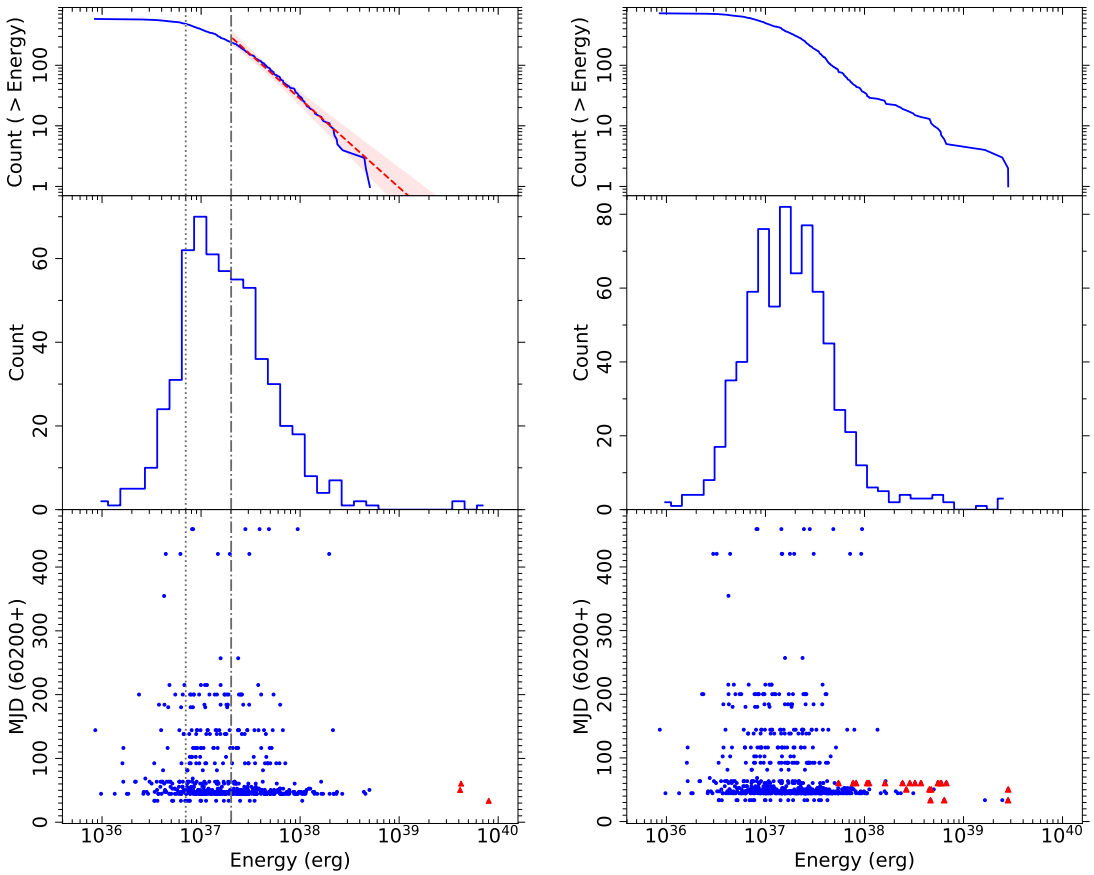


Figure 7. The energy distribution of bursts (left) and sub-bursts (right) detected from FRB 20230607A by FAST. The bottom subpanels show the time-dependent energy distribution of bursts and sub-bursts of FRB 20230607A. The triangles represent the bright bursts, while the other points correspond to weaker bursts. The gray dotted and dashed–dotted vertical lines indicate the detection threshold and completeness threshold of 7.0×10^{36} erg and 2.0×10^{37} erg (95% detection probability), respectively, for bursts with the 1 ms temporal width or 0.2 ms sampling time for the S/N = 7. The mid-subpanels show the number distribution of the sub-burst or burst of FRB 20230607A against the energy distribution of bursts. The top subpanels present the cumulative distribution of the energy function toward weak bursts. The red dashed line in the left panel for the bursts represents the best-fitted power-law function with an index of $\alpha = -2.46 \pm 0.05$ for the high-energy part with the 95% confidence interval shown in the shaded region.

subsequently used for the analysis of the burst energy and estimating the flux of a potential PRS. The isotropic-equivalent energy of a sub-burst can be estimated as

$$E = \frac{4\pi D_L^2}{(1+z)} F_\nu \mathrm{BW_e}. \quad (3)$$

The temporal energy distribution of bursts and sub-bursts for FRB 20230607A is displayed in Figure 7. The three bright bursts with substantial energies are marked in red. The detection threshold S/N > 7 (corresponding energy is $>7.0 \times 10^{36}$ erg) was calculated via the radiometer equation, while the completeness threshold ($\sim 2.0 \times 10^{37}$ erg, corresponding to 95% detection probability) was determined through mock burst injection simulations following H. Xu et al. (2022). The number distribution of the burst energy at the high-energy part can be described by a power-law function with an index of $\alpha = -2.46 \pm 0.05$, which is lower than the spectral index typically observed for pulsars (S. D. Bates et al. 2013; F. Jankowski et al. 2018).

3.5. Predicated Persistent Radio Source from FRB 20230607A

With the well measured DM and RM, we plot FRB 20230607A in the DM versus RM space along with other repeating and one-off FRBs in Figure 8. One can see that it ranks third in the measured RM values of FRBs, just behind FRB 20201122 (D. Michilli et al. 2018) and FRB 20190520B (C. H. Niu et al. 2022). The combination of RM and DM gives an average parallel magnetic field of $-42\,\mu$G, much larger than the typical interstellar magnetic field of a few μG in the Milky Way, and that of the intergalactic medium of a few nG (J. Xu & J. L. Han 2014, 2022; E. Carretti et al. 2022). Such a high magnetic field strength suggests that FRB 20230607A is located in an extremely magnetized local environment, similar to FRB 20121102A (D. Michilli et al. 2018) and FRB 20190520B (R. Anna-Thomas et al. 2023), each associated with a PRS (S. Chatterjee et al. 2017; C. H. Niu et al. 2022).

Physically, there could be a connection between RM and the luminosity of the PRS. This is because the PRS is likely powered by synchrotron radiation (Y.-P. Yang et al. 2016, 2020; K. Murase et al. 2016; B. D. Metzger et al. 2017), the brightness of which also depends on the electron number density[22] and the strength of local magnetic fields. It has been suggested that RM could be a good proxy of the PRS luminosity, with a predicted scaling law of $L_\nu \propto (\zeta_e \gamma_{\rm th}^2 R^2)|\mathrm{RM}|$ (Y.-P. Yang et al. 2020, 2022), where R is the radius of the region that

[22] Strictly speaking, it depends on the number density of relativistic electrons, which can be reasonably assumed to be proportional to the cold electron number density (Y.-P. Yang et al. 2020, 2022).

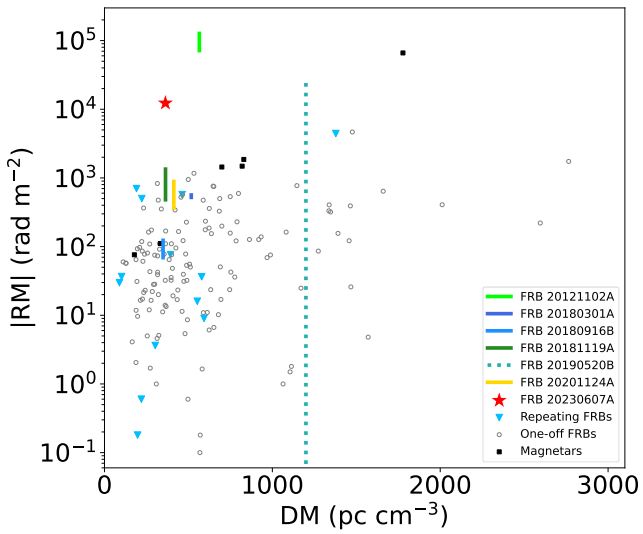


Figure 8. The observed RM vs. DM of FRBs, including FRB 20230607A from this paper, other repeating FRBs and many one-off FRBs (E. Petroff et al. 2016; S. Osłowski et al. 2019; R. Luo et al. 2020; CHIME/FRB Collaboration et al. 2021; Y. Feng et al. 2022; A. Plavin et al. 2022; H. Xu et al. 2022; R. Anna-Thomas et al. 2023; J. T. Faber et al. 2024; R. Mckinven et al. 2023a, 2023b; M. B. Sherman et al. 2023; D. J. Zhou et al. 2023; A. Pandhi et al. 2024), and magnetars (G. Hobbs et al. 2004; W. Zhu et al. 2023). The large absolute RM of FRB 20230607A implies a highly magnetized environment around the FRB source.

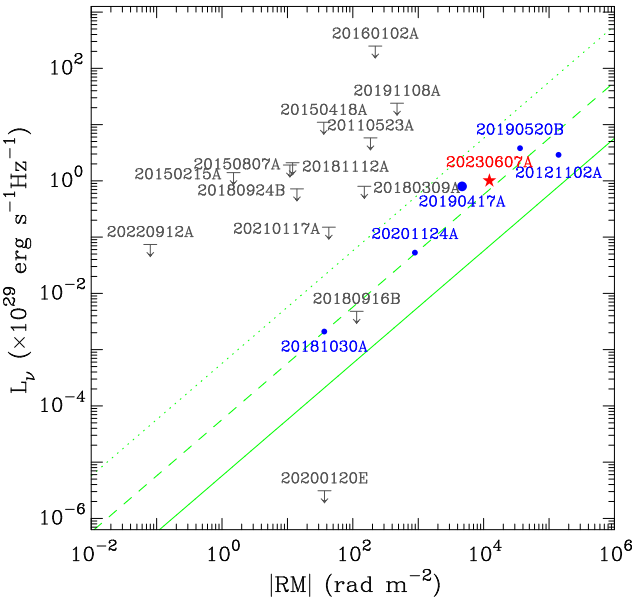


Figure 9. The RM $-$ L_ν of the observed FRBs along with the theoretical prediction of Y.-P. Yang et al. (2022). The dotted, dashed, and solid lines indicate the possible relation of $\zeta_e \gamma_{\rm th}^2 (R/0.01\ {\rm pc})^2 = 10$, 1, 0.1, respectively. The data points are listed in Table 5. The PRS of FRB 20230607A has not yet been detected. The red star indicates its predicted L_ν based on its measured RM.

contributes to the PRS and the RM, ζ_e is the electron fraction that generates synchrotron emission in the GHz band, $\gamma_{\rm th}$ the Lorentz factor defined by $\gamma_{\rm th}^2 \equiv \int n_e(\gamma) d\gamma / \int [n_e(\gamma)/\gamma^2] d\gamma$, where $n_e(\gamma)$ is the differential distribution of electrons. In particular, for an electron distribution with a thermal and a nonthermal component, $\gamma_{\rm th}$ would be the typical Lorentz factor separating the two components. Such a predicted scaling has been recently verified by the detection of several more PRSs (G. Bruni et al. 2024a; A. L. Ibik et al. 2024).

Based on the large absolute RM value of FRB 20230607A, the predicted specific luminosity of the PRS would be about $L_\nu \sim 10^{29}\,{\rm erg\,s^{-1}\,Hz^{-1}}$, as indicated in Figure 9 (the parameters of each source used are listed in Table 5 of the Appendix). At the distance $d \sim 0.98\,{\rm Gpc}$ estimated by the ${\rm DM_{IGM}}$, the maximum flux density of the PRS is around $F_\nu \sim 87\ \mu{\rm Jy}$. We encourage observers to conduct a deep search of a possible PRS associated with FRB 20230607A.

4. Conclusion and Discussion

This paper presents the observational results of FRB 20230607A by FAST. In 15.6 hr spanning 16 months, we detected 565 bursts from the source. This allowed us to perform the statistical properties of the bursts, including waiting times, temporal widths, central frequencies and frequency widths, fluences, and energies. The distributions are consistent with other well-studied repeaters observed by FAST, suggesting that active repeaters share many properties in common.

In any case, several observational properties stand out from this source. First, one of the three brightest bursts, B10, showed a unique light curve, with a bright, narrow spike lasting 0.3 ms sticking out from the surrounding broader pulses, which in general show a frequency down-drifting. It has been known that repeating FRBs tend to show broader pulses than nonrepeating ones (Z. Pleunis et al. 2021). Our observed feature suggests that repeaters can make both broad and narrow pulses. Our observation suggests that at least some apparently nonrepeating FRBs with narrow spikes could be the tip of the iceberg of an underlying repeater with fainter broader pulses.

The 0.3 ms spike also strongly suggests a magnetospheric origin of the FRB emission (W. Lu et al. 2022; B. Zhang 2023). Another strong evidence in support of such a conclusion is the narrow spectra widely observed in this source, with $\Delta\nu/\nu_0 = 0.125$, much smaller than the lower limit 0.58 predicted in the far-away models invoking relativistic shocks (A. Kumar et al. 2024).

We notice that the number of detected sub-bursts depends on observing frequency with a power-law index of -4.79 ± 0.32, which means that many more bursts could be at even lower frequencies outside the FAST band. The emission frequency bandwidth of sub-bursts is typically at 231^{+171}_{-99} MHz, similar to 277^{+122}_{-84} MHz for FRB 20201124A (D. J. Zhou et al. 2022), suggesting a possible common narrowness of the FRB bursts.

From the FAST detected bursts of FRB 20230607A, the maximum burst rate was about $149.5\,{\rm h^{-1}}$. At other observing sessions, the burst rate was lower or even there was no detection. There is no evidence for an activity periodicity like some other repeating FRBs (CHIME/FRB Collaboration et al. 2020; K. M. Rajwade et al. 2020). It is also different from some other sources which show nonstopping long-term activities (C. H. Niu et al. 2022). This suggests that repeating FRBs have diverse long-term behaviors in terms of burst rate.

Finally, FRB 20230607A has the third largest $|{\rm RM_{obs}}|$, after FRB 20121102A (D. Michilli et al. 2018) and FRB 20190520B (R. Anna-Thomas et al. 2023). Its $|{\rm RM_{obs}}|$ is also close to that of the magnetar PSR J1745-2900 near the Galactic Center (D. H. F. M. Schnitzeler et al. 2016). Based on the simple relationship between the luminosity of PRS and

$|RM_{obs}|$ (Y.-P. Yang et al. 2022), we predict that there should be a PRS with a specific luminosity of $L_\nu \sim 10^{29}$ erg s^{-1} Hz^{-1}, which could be detectable.

Acknowledgments

This work made use of the data from Five-hundred-meter Aperture Spherical radio Telescope (FAST) (https://cstr.cn/31116.02.FAST). FAST is a Chinese national mega-science facility, operated by National Astronomical Observatories, Chinese Academy of Sciences. This research is triggered by the CHIME/FRB VOEvent service. D.J.Z., J.L.H., and their NAOC group are supported by the National Natural Science Foundation of China (NSFC Nos. 12588202 and 12403059), the Chinese Academy of Sciences (No. QYZDJ-SSW-SLH021, JZHKYPT-2021-06). Y.P.Y. is supported by NSFC No. 12473047 and the National SKA Program of China (2022SKA0130100). F.Y. is supported by the NSFC No. 12203045. We thank the anonymous referee for their helpful comments.

Appendix
A Complete List of Detected Bursts and Sub-bursts of FRB 20230607A

All parameters of each burst and sub-burst analysis use the method of D. J. Zhou et al. (2022) and are listed in Table 4, which includes the TOA expressed in MJD, the S/N, the burst or sub-burst width (W or W_{sb}, in ms), the observed emission peak flux density (S_{peak}, in mJy), the fluence (F_ν, in mJy ms), the frequency of emission peak (ν_0, in MHz), the bandwidth (BW_e, in MHz), the detected emit low and high frequency (ν_{low}, ν_{high} respectively, in MHz), and the group for each burst. The fitted ν_0 is not given if it is out of the effective observation bandwidth in the range of 1031.25 MHz to 1468.75 MHz. The dynamic spectrum and burst profile for each burst are present in Figure 10, together with the energy distribution and the Gaussian fitting over the observational frequency for each sub-burst. Table 5 lists the parameters and references of each source used in Figure 9.

Table 5
FRB Sample with RM Measurements (or Upper Limits) and Flux Densities of PRS

FRB Name	RM (rad m^{-2}) (1)	L_ν (10^{29} erg s^{-1} Hz^{-1}) (2)	References
FRB 20230607A	-1.2×10^4	(predicted: 1.0)	This work
FRB 20121102A	1.4×10^5	2.1	(1, 2, 3, 4)
FRB 20190520B	-3.6×10^4	3.8	(5, 6)
FRB 20201124A	−889.5	0.053	(7, 8)
FRB 20181030A	36.6	0.0021	(9, 10)
FRB 20190417A	4681	0.797	(10, 11)
FRB 20110523A	−186.1	$<5.8^{+6.6}_{-3.7}$	(12)
FRB 20150215A	1.5	$<1.4^{+1.4}_{-0.9}$	(13)
FRB 20150418A	36	$<11^{+12}_{-7}$	(14)
FRB 20150807A	12	$<2.1^{+3.7}_{-1.8}$	(15)
FRB 20160102A	−220.6	$<249^{+112}_{-84}$	(16, 17)
FRB 20180309A	<150	$<0.8^{+1.5}_{-0.7}$	(18)
FRB 20180916B	−114.6	<0.0048	(19, 20)
FRB 20180924B	14	<0.72	(21)
FRB 20181112A	10.9	<1.91	(22)
FRB 20191108A	474	$<24^{+29}_{-16}$	(23)
FRB 20200120E	−36.9	$<3.1 \times 10^{-6}$	(24, 25)
FRB 20210117A	43	<0.15	(26)
FRB 20220912A	−0.08	<0.074	(27, 28)

Notes. (1): The observed RM of each FRB.
(2): The persistent emission luminosity.
References. (1) L. G. Spitler et al. (2014), (2) S. P. Tendulkar et al. (2017), (3) B. Marcote et al. (2017), (4) D. Michilli et al. (2018), (5) (C. H. Niu et al. 2022), (6) R. Anna-Thomas et al. (2023), (7) H. Xu et al. (2022), (8) G. Bruni et al. (2024a), (9) R. Mckinven et al. (2023b), (10) A. L. Ibik et al. (2024), (11) Y. Feng et al. (2022), (12) K. Masui et al. (2015), (13) E. Petroff et al. (2017), (14) E. F. Keane et al. (2016), (15) V. Ravi et al. (2016), (16) S. Bhandari et al. (2018), (17) M. Caleb et al. (2018), (18) S. Osłowski et al. (2019), (19) CHIME/FRB Collaboration et al. (2019), (20) B. Marcote et al. (2020), (21) K. W. Bannister et al. (2019), (22) J. X. Prochaska et al. (2019), (23) L. Connor et al. (2020), (24) M. Bhardwaj et al. (2021), (25) F. Kirsten et al. (2022), (26) S. Bhandari et al. (2023), (27) Y.-K. Zhang et al. (2023), (28) D. M. Hewitt et al. (2024).

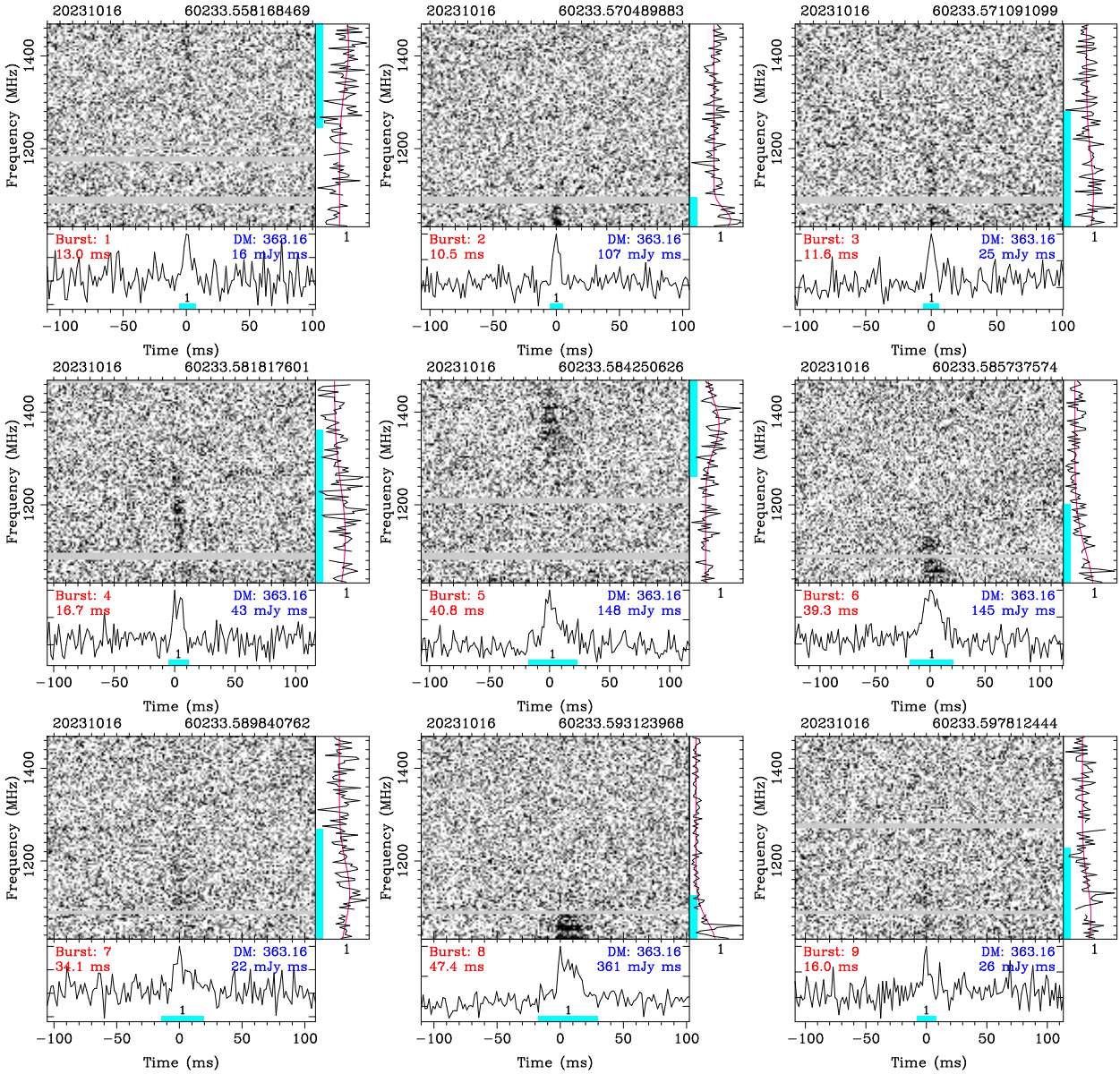


Figure 10. The dynamic spectra of each burst for FRB 20230607A. The complete figure set (565 subimages of all the bursts) is available in the online journal. (The complete figure set (566 images) is available in the online article.)

ORCID iDs

DeJiang Zhou https://orcid.org/0000-0002-6423-6106
J. L. Han https://orcid.org/0000-0002-9274-3092
Bing Zhang https://orcid.org/0000-0002-9725-2524
WeiWei Zhu https://orcid.org/0000-0001-5105-4058
Wei-yang Wang https://orcid.org/0000-0001-9036-8543
Yuan-Pei Yang https://orcid.org/0000-0001-6374-8313
Yuanhong Qu https://orcid.org/0000-0003-4721-4869
Yong-Kun Zhang https://orcid.org/0000-0002-8744-3546
Yi Yan https://orcid.org/0009-0008-1612-9948
Wei-Cong Jing https://orcid.org/0000-0002-1056-5895
Jintao Xie https://orcid.org/0000-0001-5649-2591
Xuan Yang https://orcid.org/0009-0009-3517-6640
Ye Li https://orcid.org/0000-0001-5931-2381
Dongzi Li https://orcid.org/0000-0001-7931-0607
Jia-Rui Niu https://orcid.org/0000-0001-8065-4191
Zi-Wei Wu https://orcid.org/0000-0002-1381-7859
Qin Wu https://orcid.org/0000-0001-6021-5933
Yi Feng https://orcid.org/0000-0002-0475-7479
Fayin Wang https://orcid.org/0000-0003-4157-7714
Pei Wang https://orcid.org/0000-0002-3386-7159

References

Anna-Thomas, R., Connor, L., Dai, S., et al. 2023, Sci, 380, 599
Bannister, K. W., Deller, A. T., Phillips, C., et al. 2019, Sci, 365, 565
Bates, S. D., Lorimer, D. R., & Verbiest, J. P. W. 2013, MNRAS, 431, 1352
Beniamin, P., & Kumar, P. 2020, MNRAS, 498, 651
Beniamini, P., Kumar, P., & Narayan, R. 2022, MNRAS, 510, 4654
Bhandari, S., Keane, E. F., Barr, E. D., et al. 2018, MNRAS, 475, 1427
Bhandari, S., Gordon, A. C., Scott, D. R., et al. 2023, ApJ, 948, 67
Bhardwaj, M., Gaensler, B. M., Kaspi, V. M., et al. 2021, ApJL, 910, L18
Bhusare, Y., Maan, Y., & Kumar, A. 2024, ATeL, 16820, 1
Bruni, G., Piro, L., Yang, Y.-P., et al. 2024a, Natur, 632, 1014
Bruni, G., Piro, L., Yang, Y. P., et al. 2024b, arXiv:2412.01478
Caleb, M., Keane, E. F., van Straten, W., et al. 2018, MNRAS, 478, 2046
Carretti, E., Vacca, V., O'Sullivan, S. P., et al. 2022, MNRAS, 512, 945
Chatterjee, S., Law, C. J., Wharton, R. S., et al. 2017, Natur, 541, 58

CHIME/FRB Collaboration, Amiri, M., Andersen, B. C., et al. 2020, Natur, 582, 351
CHIME/FRB Collaboration, Amiri, M., Andersen, B. C., et al. 2021, ApJS, 257, 59
CHIME/FRB Collaboration, Amiri, M., Bandura, K., et al. 2018, ApJ, 863, 48
CHIME/FRB Collaboration, Andersen, B. C., Bandura, K., et al. 2019, ApJL, 885, L24
Connor, L., van Leeuwen, J., Oostrum, L. C., et al. 2020, MNRAS, 499, 4716
Deng, W., & Zhang, B. 2014, ApJL, 783, L35
Faber, J. T., Michilli, D., Mckinven, R., et al. 2024, ApJ, 974, 274
Farah, W., Flynn, C., Bailes, M., et al. 2018, MNRAS, 478, 1209
Feng, Y., Li, D., Yang, Y.-P., et al. 2022, Sci, 375, 1266
Han, J. L., Wang, C., Wang, P. F., et al. 2021, RAA, 21, 107
Hessels, J. W. T., Spitler, L. G., Seymour, A. D., et al. 2019, ApJL, 876, L23
Hewitt, D. M., Bhandari, S., Marcote, B., et al. 2024, MNRAS, 529, 1814
Hewitt, D. M., Hessels, J. W. T., Ould-Boukattine, O. S., et al. 2023, MNRAS, 526, 2039
Hobbs, G., Manchester, R., Teoh, A., & Hobbs, M. 2004, in IAU Symp. 218, Young Neutron Stars and Their Environments, 218, ed. F. Camilo & B. M. Gaensler (San Francisco, CA: ASP), 139
Ibik, A. L., Drout, M. R., Gaensler, B. M., et al. 2024, ApJ, 976, 199
Jahns, J. N., Spitler, L. G., Nimmo, K., et al. 2023, MNRAS, 519, 666
Jankowski, F., van Straten, W., Keane, E. F., et al. 2018, MNRAS, 473, 4436
Jiang, J.-C., Wang, W.-Y., Xu, H., et al. 2022, RAA, 22, 124003
Jiang, J. C., Xu, J. W., Niu, J. R., et al. 2024, NSRev, 12, nwae293
Jiang, P., Tang, N.-Y., Hou, L.-G., et al. 2020, RAA, 20, 064
Keane, E. F., Johnston, S., Bhandari, S., et al. 2016, Natur, 530, 453
Kirsten, F., Marcote, B., Nimmo, K., et al. 2022, Natur, 602, 585
Kirsten, F., Ould-Boukattine, O. S., Herrmann, W., et al. 2024, NatAs,
Konijn, D. C., Hewitt, D. M., Hessels, J. W. T., et al. 2024, MNRAS, 534, 3331
Kumar, A., Maan, Y., & Bhusare, Y. 2024, ApJ, 977, 177
Kumar, P., Qu, Y., & Zhang, B. 2024, ApJ, 974, 160
Lanman, A. E., Andersen, B. C., Chawla, P., et al. 2022, ApJ, 927, 59
Li, D., Wang, P., Zhu, W. W., et al. 2021, Natur, 598, 267
Li, Z., Gao, H., Wei, J. J., et al. 2020, MNRAS, 496, L28
Lorimer, D. R., Bailes, M., McLaughlin, M. A., Narkevic, D. J., & Crawford, F. 2007, Sci, 318, 777
Lu, W., Beniamini, P., & Kumar, P. 2022, MNRAS, 510, 1867
Luo, R., Wang, B. J., Men, Y. P., et al. 2020, Natur, 586, 693
Macquart, J. P., Prochaska, J. X., McQuinn, M., et al. 2020, Natur, 581, 391
Marcote, B., Nimmo, K., Hessels, J. W. T., et al. 2020, Natur, 577, 190
Marcote, B., Paragi, Z., Hessels, J. W. T., et al. 2017, ApJL, 834, L8
Masui, K., Lin, H.-H., Sievers, J., et al. 2015, Natur, 528, 523
Mckinven, R., Gaensler, B. M., Michilli, D., et al. 2023a, ApJ, 950, 12
Mckinven, R., Gaensler, B. M., Michilli, D., et al. 2023b, ApJ, 951, 82
Metzger, B. D., Berger, E., & Margalit, B. 2017, ApJ, 841, 14
Michilli, D., Seymour, A., Hessels, J. W. T., et al. 2018, Natur, 553, 182
Murase, K., Kashiyama, K., & Mészáros, P. 2016, MNRAS, 461, 1498
Nan, R. 2006, ScChG, 49, 129
Nimmo, K., Hessels, J. W. T., Keimpema, A., et al. 2021, NewA, 5, 594
Nimmo, K., Hessels, J. W. T., Kirsten, F., et al. 2022, NatAs, 6, 393
Niu, C. H., Aggarwal, K., Li, D., et al. 2022, Natur, 606, 873
Niu, J. R., Wang, W. Y., Jiang, J. C., et al. 2024, ApJL, 972, L20
Niu, J.-R., Zhu, W.-W., Zhang, B., et al. 2022, RAA, 22, 124004
Osłowski, S., Shannon, R. M., Ravi, V., et al. 2019, MNRAS, 488, 868
Pandhi, A., Pleunis, Z., Mckinven, R., et al. 2024, ApJ, 968, 50
Petroff, E., Barr, E. D., Jameson, A., et al. 2016, PASA, 33, e045
Petroff, E., Burke-Spolaor, S., Keane, E. F., et al. 2017, MNRAS, 469, 4465
Planck Collaboration, Aghanim, N., Akrami, Y., et al. 2020, A&A, 641, A6
Plavin, A., Paragi, Z., Marcote, B., et al. 2022, MNRAS, 511, 6033
Pleunis, Z., Good, D. C., Kaspi, V. M., et al. 2021, ApJ, 923, 1
Prochaska, J. X., Macquart, J.-P., McQuinn, M., et al. 2019, Sci, 366, 231
Purcell, C. R., Van Eck, C. L., West, J., Sun, X. H., & Gaensler, B. M. 2020, RM-Tools: Rotation measure (RM) synthesis and Stokes QU-fitting, Astrophysics Source Code Library, ascl:2005.003
Qu, Y., & Zhang, B. 2023, MNRAS, 522, 2448
Qu, Y., & Zhang, B. 2024, ApJ, 972, 124
Rajwade, K. M., Mickaliger, M. B., Stappers, B. W., et al. 2020, MNRAS, 495, 3551
Ravi, V., Law, C. J., Li, D., et al. 2022, MNRAS, 513, 982
Ravi, V., Shannon, R. M., Bailes, M., et al. 2016, Sci, 354, 1249
Schnitzeler, D. H. F. M., Eatough, R. P., Ferrière, K., et al. 2016, MNRAS, 459, 3005
Sherman, M. B., Connor, L., Ravi, V., et al. 2024, ApJ, 964, 131
Snelders, M. P., Nimmo, K., Hessels, J. W. T., et al. 2023, NatAs,
Spitler, L. G., Cordes, J. M., Hessels, J. W. T., et al. 2014, ApJ, 790, 101
Tendulkar, S. P., Bassa, C. G., Cordes, J. M., et al. 2017, ApJL, 834, L7
Thornton, D., Stappers, B., Bailes, M., et al. 2013, Sci, 341, 53
Wang, P. F., Han, J. L., Xu, J., et al. 2023, RAA, 23, 104002
Wang, W.-Y., Yang, Y.-P., Li, H.-B., Liu, J., & Xu, R. 2024, A&A, 685, A87
Wu, Z., Zhu, W., Zhang, B., et al. 2024, ApJL, 969, L23
Wu, Z.-W., Main, R. A., Zhu, W.-W., et al. 2024, SCPMA, 67, 219512
Xu, H., Niu, J. R., Chen, P., et al. 2022, Natur, 609, 685
Xu, J., & Han, J. L. 2014, MNRAS, 442, 3329
Xu, J., & Han, J. L. 2022, ApJ, 926, 65
Yang, Y.-P. 2023, ApJ, 956, 67
Yang, Y.-P., Li, Q.-C., & Zhang, B. 2020, ApJ, 895, 7
Yang, Y.-P., Lu, W., Feng, Y., Zhang, B., & Li, D. 2022, ApJL, 928, L16
Yang, Y.-P., Zhang, B., & Dai, Z.-G. 2016, ApJL, 819, L12
Yao, J. M., Manchester, R. N., & Wang, N. 2017, ApJ, 835, 29
Zhang, B. 2022, ApJ, 925, 53
Zhang, B. 2023, RvMP, 95, 035005
Zhang, S. B., Wang, J. S., Yang, X., et al. 2024, NatCo, 15, 7454
Zhang, X., & Yu, W. 2024, ATeL, 16695, 1
Zhang, X., Yu, W., Yan, Z., Xing, Y., & Zhang, B. 2025, arXiv:2501.14247
Zhang, Y.-K., Li, D., Zhang, B., et al. 2023, ApJ, 955, 142
Zhang, Y.-K., Wang, P., Feng, Y., et al. 2022, RAA, 22, 124002
Zhou, D. J., Han, J. L., Xu, J., et al. 2023, RAA, 23, 104001
Zhou, D. J., Han, J. L., Zhang, B., et al. 2022, RAA, 22, 124001
Zhu, W., Xu, H., Zhou, D., et al. 2023, SciA, 9, eadf6198